

Watt-level coherent microwave emission from dissipation engineered solid-state quantum batteries

Yuanjin Wang,¹ Hao Wu,^{1,*} Mark Oxborrow,² and Qing Zhao^{1,†}

¹*Center for Quantum Technology Research and Key Laboratory of Advanced Optoelectronic Quantum Architecture and Measurements (MOE), School of Physics, Beijing Institute of Technology, Beijing 100081, China*

²*Department of Materials and London Centre for Nanotechnology, Imperial College London, SW7 2AZ London, United Kingdom*

(Dated: December 5, 2025)

Recently proposed metastability-induced quantum batteries have shown particular promise for coherent microwave generation. However, achieving high-power coherent microwave generation in quantum batteries remains fundamentally challenging due to quantum correlations, aging, and self-discharging processes. For the cavity-quantum-electrodynamics (CQED)-based quantum batteries, a further trade-off arises between strong spin-photon coupling for energy storage and sufficient output coupling for power delivery. To overcome these constraints, we introduce dissipation engineering as a dynamic control strategy that temporally separates energy storage and release. By suppressing emission during charging and rapidly enhancing the output coupling during discharging, we realize nanosecond microwave bursts with watt-level peak power. By optimizing three dissipation schemes, we improve work extraction efficiency of the quantum battery by over two orders of magnitude and achieve high power compression factors outperforming the state-of-the-art techniques, establishing dissipation engineering as a pathway toward room-temperature, high-power coherent microwave sources.

I. INTRODUCTION

Quantum batteries, using quantum systems for efficient storage and controlled release of energy, represent a straightforward application scenario of quantum thermodynamics[1]. Despite rapid theoretical progress[2] and various proposed experimental platforms (e.g., nuclear/electronic spins[3–5], superconducting qubits[6], ultracold atoms[7] and organic excitons[8, 9]), demonstrations of useful functionalities of quantum batteries remain scarce. In particular, their integration into practical devices for energy conversion and power generation has only begun to be explored[10, 11].

Coherent microwave generation is vital for quantum information processing, where various quantum systems, such as the superconducting circuits[12], neutral atoms[13], trapped ions[14], and optically active defect centers in solids[15, 16], require high-standard microwave control and readout mechanisms[17]. Recently, a metastability-induced quantum battery architecture was proposed as a promising route for coherent microwave generation by exploiting the masing process of the charged battery under ambient conditions[18]. The maser oscillator powered by the quantum battery not only bridges fundamental concepts of quantum thermodynamics and applications in quantum electronics, but also offers the intrinsic advantage of low-phase-noise microwave generation[19] due to the high coherence of the emitted photons and stable spin transitions in the battery.

In addition to coherence, the power scalability of the aforementioned quantum oscillator up to watt levels is also crucial for fast manipulation[17, 20–22] and high-fidelity readout[23–26] of the microwave-based quantum systems. However, the realization of high-power coherent microwave generation faces fundamental challenges in the quantum battery system. The central difficulty lies in efficiently converting stored energy into coherent radiation, a process limited by correlations[27, 28], aging[29], and self-discharging[30, 31]. Moreover, for the oscillator that relies on the cavity quantum electrodynamics (CQED) mechanism, there is a trade-off between maintaining strong spin-photon coupling for efficient energy storage and enabling sufficient outcoupling for power delivery[32, 33]. If the cavity quality factor (Q) is too high, the stored inversion cannot be efficiently released; if it is too low, premature emission prevents the battery from accumulating enough energy for high-power operation. This tension, well known in laser and maser physics, also becomes critical for quantum batteries, where both energy storage and power extraction must be optimized simultaneously.

Within this context, dissipation engineering[34, 35] has emerged as a powerful tool for controlling energy flow in CQED systems by tailoring the system-environment coupling. This concept has recently gained significant attention in the field of nonlinear optics for the generation of non-Hermitian[36] and dark pulse[37] combs, where the dissipation engineering was employed for introducing non-reciprocity or mitigating unnecessary nonlinear dynamics of energy flow.

In this work, we extend the concept of dissipation engineering from controlling nonlinear optical processes to modulating the discharge dynamics of quantum batteries. Specifically, we integrate a solid-state quantum battery

* hao.wu@bit.edu.cn

† qzhaoyuping@bit.edu.cn

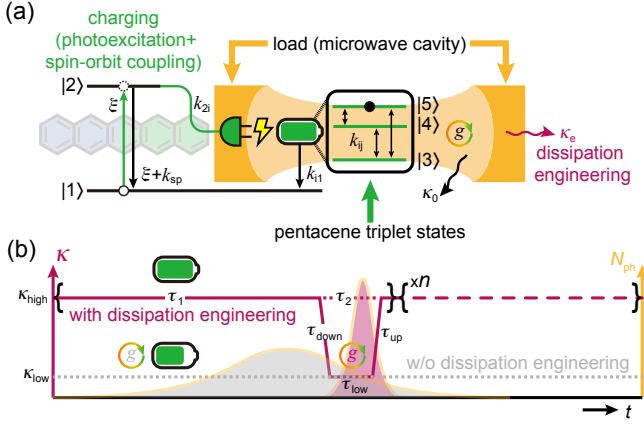


FIG. 1. (a) Schematic diagram of the charging and working mechanisms of the metastability-induced quantum battery. Dissipation engineering is realized by modulating the external coupling rate κ_e of the microwave cavity. (b) Concept of using dissipation engineering for modulating the coherent microwave generation from the quantum battery. N_{ph} , microwave photon number.

with a microwave cavity to form a maser oscillator and design a controlled discharge system that efficiently releases stored microwave photons into the external environment. We investigate three different dissipation schemes for identifying the optimal modulation strategy in terms of the coherent microwave emission power. We show that with appropriate design of the modulation parameters including the modulation duration, minimum dissipation rate, and delay time, all three schemes are capable of generating nanosecond pulses with significantly increased output power up to watt levels. These results reveal the tunability of the discharge process of quantum batteries via dissipation engineering and lay the foundation for realizing high-power microwave coherent generation using dynamical CQED control approaches.

II. SYSTEM AND CONCEPT OF DISSIPATION ENGINEERING

The working principle of the quantum battery-powered maser oscillator is shown in Fig.1(a). The quantum battery is constituted by the metastable photoexcited triplet electron spins of the pentacene molecules doped in a crystalline *p*-terphenyl matrix[18]. Photoexcitation of the pentacene molecules in the ground singlet state $|1\rangle$ to the excited singlet state $|2\rangle$, combined with the spin-orbit-coupling-induced intersystem crossing from $|2\rangle$ to the metastable triplet state can be considered as the charging process of the battery. In absence of the external magnetic field, the triplet spins possess three non-degenerate sublevels, denoted by $|3\rangle$, $|4\rangle$ and $|5\rangle$, due to the dipolar interactions. The sublevels $|3\rangle$ and $|5\rangle$ with a transition frequency ω_{35} around 1.45 GHz, characterized by the

zero-field-splitting parameters[38], are considered as the states of the quantum battery for the energy storage and extraction. The work extraction manifests as the masing process when the charged quantum battery (i.e., the sublevel $|5\rangle$ is overpopulated) is coupled to a microwave cavity whose electromagnetic mode frequency $\omega_m = \omega_{35}$. The coupling can be quantified using the spin-photon coupling strength g . The complete process of the pentacene triplet mechanism for coherent microwave generation via masing can be found in the seminal work[39].

As an open quantum system, the battery can dissipate energy via the depopulation to $|1\rangle$ and spin-lattice relaxations within the triplet sublevels. The energy extracted from the battery to the load, i.e., the cavity, can also dissipate due to the intrinsic cavity loss and the external coupling for detecting the microwave photons generated in the cavity. The two dissipation channels with the respective rates κ_0 and κ_e contribute to the total dissipation of the cavity, of which the rate can be characterized as $\kappa = \kappa_0 + \kappa_e$. κ_0 is influenced by the ohmic and dielectric properties of the microwave cavity, whereas κ_e is determined by the output coupling coefficient.

In this system, dissipation engineering is realized by dynamically modulating the external coupling rate κ_e , which results in the time-dependent variation of the total dissipation rate κ , as shown in Fig.1(b). In general, for realistic pentacene maser platforms[32, 39, 40], the quantum battery is coupled with a high- Q (low- κ) cavity continuously. The low dissipation of the cavity helps accumulate microwave photons and facilitates the stimulated emission of the quantum battery due to the presence of the spin-photon coupling. Thus, the work extraction occurs simultaneously with the charging process when the battery is not fully charged, leading to a relatively long-lasting and weak microwave emission.

In contrast, by exploiting dissipation engineering, the work extraction can take place when the battery is fully charged, prior to which the cavity dissipation is set to a high value (κ_{high}) for a certain period τ_1 , so that the spin-photon coupling does not play important roles in the discharging of the battery. Moreover, the duration of work extraction can be manipulated by the period τ_2 during which the cavity dissipation is switched to a low value (κ_{low}) that sustains for a period τ_{low} before recovery to κ_{high} . In principle, by compressing the interaction time between the fully charged quantum battery and cavity to a limited value (e.g., τ_2), more battery energy can be employed for coherent microwave generation and the microwave pulse width can be substantially narrowed, leading to the enhanced output power. The complete cycle comprising τ_1 and τ_2 can be repetitive for generating microwave pulse trains. The above modulation approach is analogous to the so-called repetitive *Q*-switching technique[41] widely used for high-power pulsed lasers but with a distinct dissipation channel. Instead of introducing modulated *internal* loss of the cavity, we focus on the control of *external* coupling which directly connects to the microwave output characteristics.

By taking practical feasibility into account, we investigate the effects of three different schemes of dissipation engineering in coherent microwave generation, which are called the *instantaneous*, *linear*, and *sinusoidal* schemes. The difference arises from the manner of the switching between the κ_{high} and κ_{low} states, as shown in Fig.1(b), since in reality, the switching normally takes a certain time that depends on the performance of the switching hardware components (e.g., the solid-state microwave switches) and the ringing behaviors of cavities. The instantaneous scheme demonstrates an ideal case that there are no transition phases between the κ_{high} and κ_{low} states, resulting in $\tau_2 = \tau_{\text{low}}$. For the linear scheme, the switching is accomplished with the transition phases τ_{down} and τ_{up} . During τ_{down} , the total dissipation reduces linearly according to the formula $\kappa = \kappa_{\text{high}} - (\kappa_{\text{high}} - \kappa_{\text{low}}) \times \Delta t / \tau_{\text{down}}$, where Δt is the time elapsed during the descent of κ from its maximum value κ_{high} ($\Delta t \leq \tau_{\text{down}}$). Subsequently, the dissipation increases during phase τ_{up} , following a trajectory that is a reverse of phase τ_{down} ($\tau_{\text{down}} = \tau_{\text{up}}$). For the sinusoidal scheme, instead of implementing the linear transition phases, the dissipation varies sinusoidally, for instance, the dissipation in phase τ_{down} varies according to the expression $\kappa = \kappa_{\text{high}} - (\kappa_{\text{high}} - \kappa_{\text{low}}) \times \sin^2(\pi \Delta t / (2 \times \tau_{\text{down}}))$. Similarly, the variation in phase τ_{up} shows an opposite trend to that in phase τ_{down} .

III. MODEL

We employ the reduced density operator $\hat{\rho}$ to represent the state of the metastable quantum battery, whose dynamical evolution is described by the following master equation[32, 42]:

$$\partial_t \hat{\rho} = -\frac{i}{\hbar} [\hat{H}_{\text{bat}} + \hat{H}_{\text{m}} + \hat{H}_{\text{m-bat}}, \hat{\rho}] + \mathcal{L}[\hat{\rho}], \quad (1)$$

where the Hamiltonian of the quantum battery $\hat{H}_{\text{bat}} = \frac{1}{2} \hbar \omega_{35} \sum_{k=1}^{N_{\text{pen}}} (\hat{\sigma}_k^{55} - \hat{\sigma}_k^{33})$. Here, \hbar , k , and N_{pen} are respectively the reduced Planck constant, the individual pentacene molecule, and the total number of pentacene molecules. $\hat{\sigma}_k^{ij} = |i_k\rangle \langle j_k|$ is the spin transition operator. The Hamiltonian of the microwave cavity $\hat{H}_{\text{m}} = \hbar \omega_{\text{m}} \hat{a}^\dagger \hat{a}$, where \hat{a}^\dagger (\hat{a}) is the creation (annihilation) operator. The interaction between the quantum battery and the microwave cavity can be expressed by the Hamiltonian $\hat{H}_{\text{m-bat}} = \hbar \sum_k g_{35} (\hat{\sigma}_k^{53} \hat{a} + \hat{a}^\dagger \hat{\sigma}_k^{35})$ with the coupling strength g_{35} . $\mathcal{L}[\hat{\rho}]$ is the Liouvillian, which accounts for the dissipative processes in the system.

The full dynamics including all components of the Liouvillian can be found in Appendix A, where the dissipation engineering is performed in the component describing the microwave photon loss in the cavity mode:

$$\mathcal{L}_{\text{m}}[\hat{\rho}] = \frac{\kappa}{2} [(n_{\text{m}}^{\text{th}} + 1) \mathcal{D}[\hat{a}] \hat{\rho} + n_{\text{m}}^{\text{th}} \mathcal{D}[\hat{a}^\dagger] \hat{\rho}], \quad (2)$$

where the Lindblad superoperator $\mathcal{D}[\hat{O}] \hat{\rho} = 2\hat{O} \hat{\rho} \hat{O}^\dagger - \hat{O}^\dagger \hat{O} \hat{\rho} - \hat{\rho} \hat{O}^\dagger \hat{O}$ and the thermal occupation number for temperature T is defined by $n_{\text{m}}^{\text{th}} = [\exp(\frac{\hbar \omega_{\text{m}}}{k_{\text{B}} T}) - 1]^{-1}$ with k_{B} the Boltzmann constant, which is approximately 4000 at room temperature.

By performing the mean-field calculations of the coupled differential equations derived from the master equation (see Appendix A), the stored energy of the quantum battery can be expressed as $E(t) = N_{\text{pen}} \hbar \omega_{35} \langle \hat{\sigma}_1^{55}(t) \rangle$. Let $P_{\text{ins}}(t) = \dot{E}(t)$ be the instantaneous power of the quantum battery. Meanwhile, to quantify the process of the work extraction, the useful energy $E_{\text{ph}}(t)$ extracted from the quantum battery for coherent microwave generation can be expressed with the number of intra-cavity microwave photons $N_{\text{ph}}(t) = \langle \hat{a}^\dagger \hat{a} \rangle(t)$ as $E_{\text{ph}}(t) = N_{\text{ph}}(t) \hbar \omega_{\text{m}}$. And the microwave output power is calculated using the formula

$$P_{\text{out}}(t) = N_{\text{ph}}(t) \hbar \omega_{\text{m}} \kappa k_{\text{c}} / (1 + k_{\text{c}}), \quad (3)$$

where k_{c} is the coupling coefficient characterizing the output coupler of the cavity and defined as[43]

$$k_{\text{c}} = \frac{\kappa_{\text{e}}}{\kappa_0} = \frac{\kappa}{\kappa_0} - 1. \quad (4)$$

IV. CONTROLLABLE MICROWAVE PULSE GENERATION

By simulating the temporal evolution of the microwave photon number N_{ph} in the cavity under the three dissipation-engineering protocols, as shown in Fig.2(a)-(c), we first verify the concept of dissipation engineering for controllable microwave pulse generation. As predicted, these schemes effectively modulate the coupling between the cavity field and the external environment, thereby shaping the dynamics of photon accumulation and release during each discharging cycle of the quantum battery.

In the instantaneous scheme, the abrupt switching of κ simulates an ideal process, where energy stored in the quantum battery is suddenly extracted into the cavity mode and then immediately 'used' via the external coupling. This rapid energy extraction leads to sharply defined microwave pulses with well-controlled intensity and interval, which are indicated by the overlaps between the bursts of intra-cavity photon number (N_{ph}) and the modulation of dissipation in terms of the onset and termination positions. By contrast, in the linear and sinusoidal schemes, κ changes continuously in time, producing a more gradual transition between the energy extraction and usage stages. As a result, the photon number continues to rise slightly even after reaching to the maximum obtained in the instantaneous scheme, reflecting a delayed energy extraction caused by the finite rate of dissipation engineering. This behavior mirrors the finite response of an oscillator under time-dependent dissipation engineering in realistic devices[44].

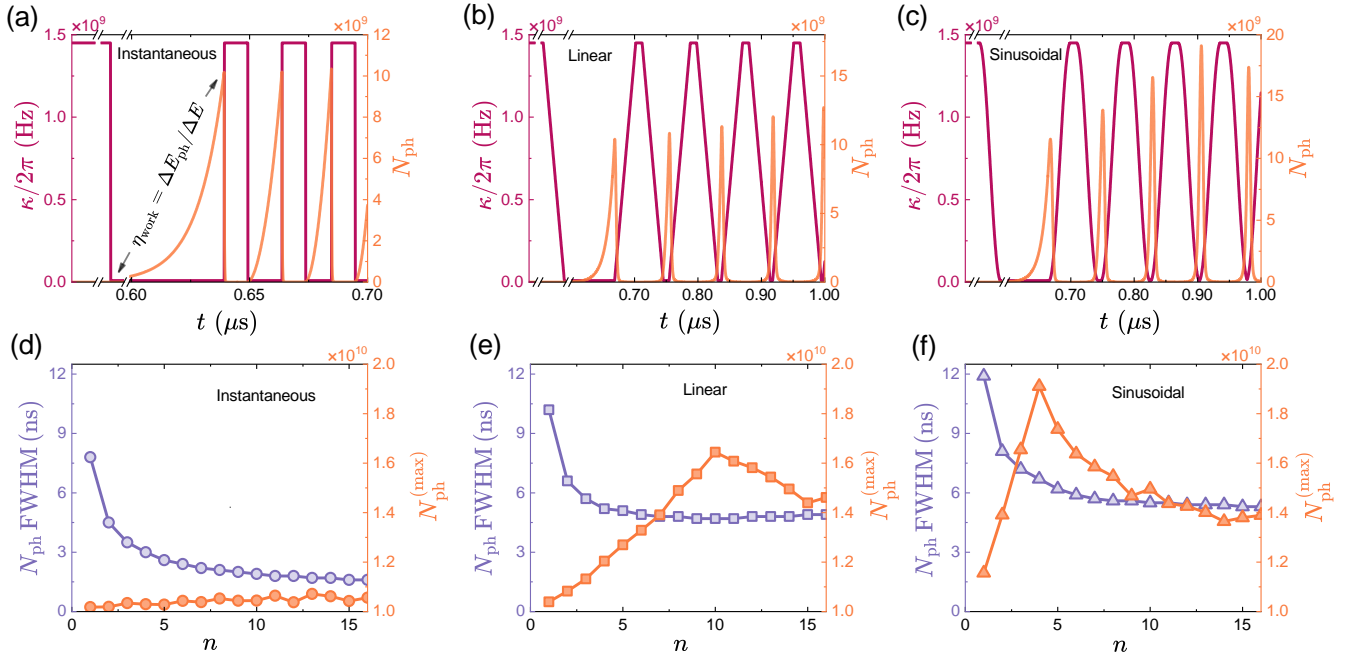


FIG. 2. (a-c) Temporal evolution of the cavity total dissipation rate κ (left axis) and the microwave photon number N_{ph} (right axis) under three dissipation-engineering protocols. The τ_{low} stage ends once the photon number reaches the threshold $N_{\text{ph}} = 10^{10}$, after which the dissipation resets for the next cycle. The work extraction efficiency η_{work} is defined as the ratio between the photon energy change ΔE_{ph} and the quantum battery energy change ΔE during each emission event, calculated from the start of the τ_2 stage to the peak photon number. (d-f) Evolution of the full width at half maximum (FWHM, left axis) and maximum photon number $N_{\text{ph}}^{(\text{max})}$ (right axis) for successive (the n th) microwave pulses under the three modulation schemes. All simulations were performed with $\tau_1 = 10^{-8}$ s, $\kappa_{\text{low}}/2\pi = 9.55 \times 10^6$ Hz, $\tau_{\text{down}} = 2/\kappa_{\text{low}}$, and $\tau_{\text{up}} = \tau_{\text{down}}$. Additional system parameters are presented in Table 1 of Appendix B. Unless otherwise stated, all simulations adopt identical system parameters.

Figs.2(d)-(f) summarize the evolution of the full width at half maximum (FWHM) and the maximum intra-cavity photon number $[N_{\text{ph}}^{(\text{max})}]$ of successive pulses. For all schemes, the FWHM narrows rapidly during the first few cycles and subsequently stabilizes. The reduction in pulse width arises from the growing initial photon number at the onset of each τ_2 stage (see Fig.S1 in Appendix B). As the cavity stores emitted/residual photons between cycles, the field buildup becomes progressively faster in subsequent emissions, producing shorter and more intense pulses. Such effects have been proved by the seeding measurements in the room-temperature pulsed maser device[45]. Eventually, as the growing self-seeded photons enable to saturate the maser transition, the FWHM tends to stabilize or even broaden, for instance, in the linear scheme.

Quantitatively, all three schemes compress the microwave pulses into the nanosecond regime, which is approximately three orders of magnitude narrower than the so far shortest maser pulse obtained at room temperature[45]. Under the instantaneous modulation, the FWHMs of successive pulses decrease from 8 ns to below 2 ns, whereas the minimum FWHM around 5 ns is obtained in both linear and sinusoidal schemes. This difference can be attributed to the gradual modulations of κ that allow partial energy leakage of the quantum

battery in form of microwave emission during the phase τ_{down} and extend the emission tail during the phase τ_{up} , thus limiting the achievable pulse compression.

The maximum intra-cavity photon number of each pulse exhibits fluctuations around the preset threshold $N_{\text{ph}} = 10^{10}$, which is imposed to prevent the FWHM broadening caused by excessive energy release per pulse. Since the threshold defines when the dissipation switching starts, the resulted τ_{low} varies from cycle to cycle. For all schemes, τ_{down} of the first cycle typically lasts longer as shown in Fig.2(a)-(c) due to the initially less populated cavity, while later cycles proceed faster once residual photons act as a seed field. Among all schemes, the instantaneous scheme yields the most stable pulse trains, as its abrupt switching minimizes the influence of residual photons on the subsequent emission. In contrast, due to the prolonged spin-photon coupling during the smooth transition phases in the linear and sinusoidal modulations, the overall behavior of $N_{\text{ph}}^{(\text{max})}$ shows a significant growth beyond the threshold with a non-monotonic trend. After reaching the maximums at respectively the 10th and 4th cycles of the linear and sinusoidal schemes, $N_{\text{ph}}^{(\text{max})}$ of the subsequent pulses gradually drops to a quasi-stable value at 1.4×10^{10} . This occurs because, after the 10th cycle, the linear scheme achieves the target photon number of 10^{10} already during phase τ_{down} , proceeds directly

to phase τ_{up} , and does not undergo a complete phase τ_{up} , resulting in a decrease in photon number. A similar behavior is observed with the sinusoidal scheme, where the photon number reaches 10^{10} during phase τ_{down} after the 4th cycle. (see Fig.S1(b) in Appendix B)

V. MICROWAVE OUTPUT PERFORMANCE

In addition to the analysis of the microwave generation inside the cavity, we also implement the simulation of the microwave output from the cavity based on Eqs.(3) and (4). The temporal evolution of the output power P_{out} under the three dissipation modulation protocols is shown in Figs.3(a)–(c). To help analyze the output performance, the instantaneous power P_{ins} indicating the time-dependence of the energy storage in the quantum battery is illustrated as well. The power stability of the output pulse trains obtained with the three schemes is similar to that of the intra-cavity photon number shown in Fig.2. The results demonstrate that the instantaneous scheme offers the possibility of achieving the most stable output pulses since the beginning of the dissipation modulation, whereas it takes several cycles for the other two schemes to stabilize the output. It is worth noting that the output pulses obtained with the sinusoidal modulation protocol start to become stable prior to those in the linear scheme, similar to the trend of reaching the peak of $N_{\text{ph}}^{(\text{max})}$ in the linear and sinusoidal schemes, where the maximum photon numbers are established respectively in the 10th and 4th cycles as shown in Figs.2(e) and 2(f). Despite the decline of $N_{\text{ph}}^{(\text{max})}$ after reaching the maximums in both schemes, the later-stage stability indicates the output power is more sensitive to the variation of the intra-cavity photon number when the cavity is less populated in the early stage.

In terms of the magnitude of P_{out} , with the non-optimal parameter setting, all schemes can lead to microwatt (μW)-level output power which is of the same order of magnitude as that of most experimentally demonstrated pentacene masers[32, 39, 40, 45–47]. We note that the very recent experimental realizations show the possibility of reaching the milliwatt (mW) level with a much stronger optical pumping[48, 49]. Among them, the instantaneous scheme gives rise to the maximum output power, while its intra-cavity photon number is the lowest (just above the preset threshold) in Fig.2. The phenomenon can be explained by evaluating the instantaneous power P_{ins} shown in Figs.3(a)–(c). Before the initialization of the modulation, the rise of P_{ins} under all schemes arises from the charging process. Note that, due to the denser pulses, the time scale used for plotting P_{ins} of the instantaneous scheme is different from those in the other two schemes so that the dramatic increase of P_{ins} is not shown in Fig.3(a). Upon work extraction, it can be found that for the first cycle, all schemes demonstrate almost the same level of P_{ins} , indicating the energy extracted from the battery for the microwave generation is similar. Because of the

energy conservation, the more microwave photons coupled out of the cavity results in the fewer intra-cavity photons. Moreover, the instantaneous scheme shows the relatively stable P_{ins} over the pulse trains, where significant decrease is observed for the other two schemes in later cycles. According to the magnified views of Figs.3(a)–(c), the power losses are attributed to the continuously increased photon leakage between cycles, where the transition regimes of the dissipation switching are present in both schemes.

In addition to the output power, the output pulse width is also crucial for practical applications. Figs.3(d)–(f) show the evolution of the FWHM of the output pulses for each scheme. Strikingly, by employing the ideal dissipation engineering, i.e., the instantaneous protocol, the output pulse widths can be drastically reduced to tens of picoseconds, which are two orders of magnitudes narrower compared to those obtained with the other protocols. Again, the broader output pulses at the level of nanoseconds result from the transition regimes in the linear and sinusoidal schemes. In contrast to the FWHM of N_{ph} shown in Fig.2, which presents a decrease trend in the initial pulses due to the buildup of cavity field, the FWHM of P_{out} is relatively stable over the successive pulses and narrower. This may be attributed to dissipation engineering which largely isolates the output channels from the intra-cavity dynamics and thus the output pulse shape is governed by the modulation behaviors.

We further evaluate the efficiency of coherent microwave pulse generation with dissipation engineering. We define the work extraction efficiency $\eta_{\text{work}} = \Delta E_{\text{ph}} / \Delta E$ with the intra-cavity photon energy change ΔE_{ph} and the quantum battery energy change ΔE during each cycle. For consistency among the three schemes, the period chosen for the calculation starts from the onset of τ_2 to the position where $N_{\text{ph}}^{(\text{max})}$ is reached in each cycle, as illustrated in Fig.2(a). As shown in Fig.3(g)–(i), the instantaneous protocol achieves the highest η_{work} , benefiting from the abrupt release of stored energy that against the non-radiative losses[50] of the pentacene triplet spins. In contrast, the linear and sinusoidal modulations yield similar, but lower efficiencies because of the partial loss of the battery energy during the gradual modulation of κ . In the first few cycles, η_{work} remains small in all schemes due to the initial low photon number at the start of the τ_2 stage, where the ohmic and dielectric dissipation[43] of the cavity, constituting the internal dissipation (κ_0), dominates over the stimulated emission. As the cavity field builds up after several cycles, η_{work} increases and eventually saturates following the similar trend of $N_{\text{ph}}^{(\text{max})}$. We note that with the current parameter setting, the overall η_{work} of the order of 10^{-3} is rather low, of which the optimization will be presented in the next section.

Moreover, we investigate the power compression factor η_{power} of different modulation protocols, which is a quantity employed in the field of (sub)nanosecond microwave pulse generation[51, 52], to characterize how effectively a long-duration, low-power input pulse is converted into a short-duration, high-power output pulse. In our case,

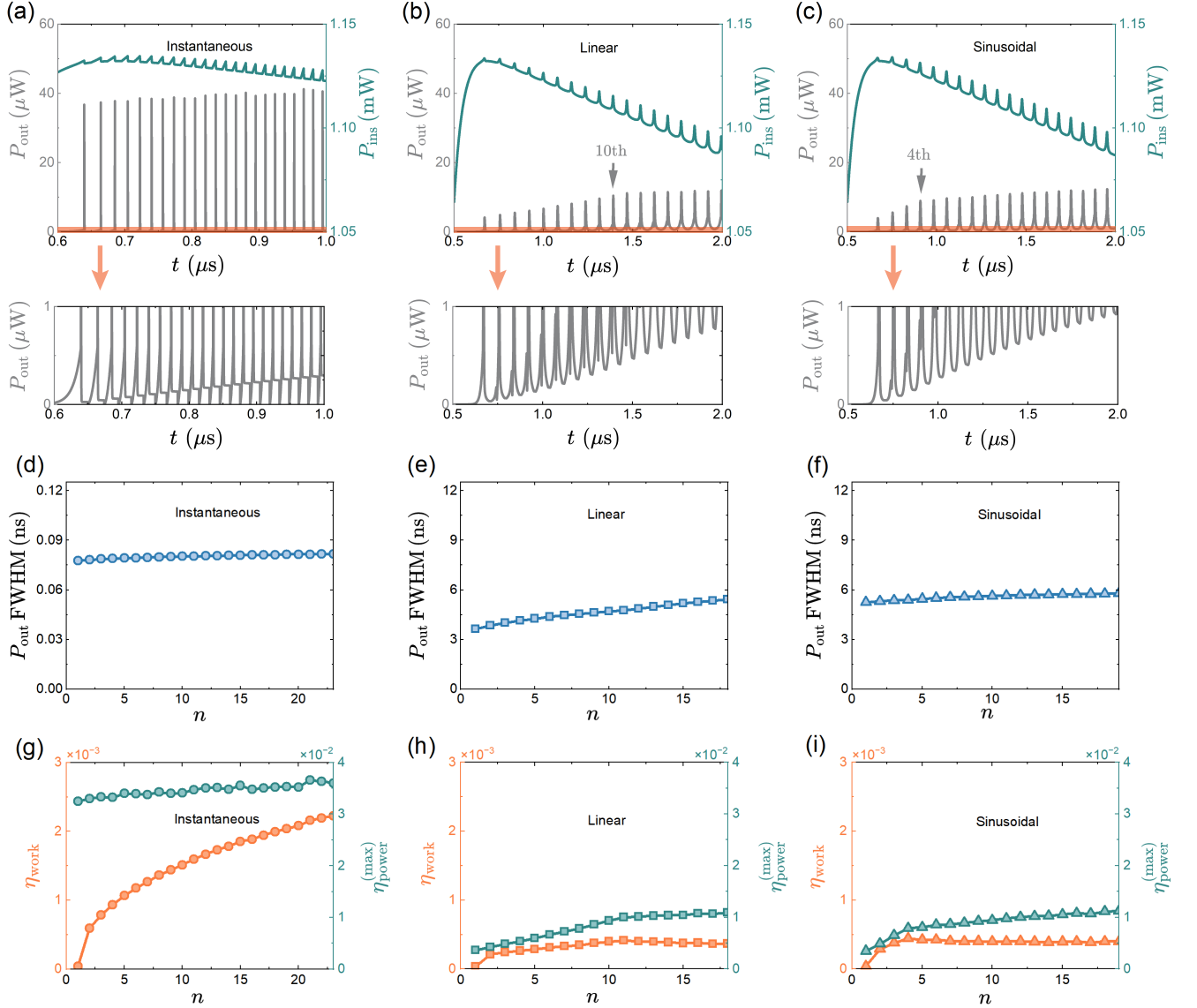


FIG. 3. (a-c) Temporal evolution of the output power P_{out} (left axis) and instantaneous power P_{ins} (right axis) under the three dissipation-engineering schemes. For clarity, the time scale in (a) is different from those in (b) and (c). The insets show magnified views of P_{out} within the organic shadow regimes. (d-f) Evolution of the FWHM of the output power P_{out} as well as (g-i) the work extraction efficiency η_{work} (left axis) and maximum power compression factor $\eta_{\text{power}}^{(\text{max})}$ (right axis, power compression factor at the maximum output power) for successive (the n th) microwave pulses under the three modulation schemes

there are no microwave pulses injected in the cavity, instead, the pulsed discharging from the quantum battery can be considered as the 'input' source, linking the microwave output power P_{out} to the instantaneous power P_{ins} of the quantum battery. Figs.3(g)-(i) illustrate the maximum power compression factors $\eta_{\text{power}}^{(\text{max})}$ in the three schemes that is calculated by the ratio of P_{out} to P_{ins} at the maximum output power in each cycle shown in Figs.3(a)-(c). Similar to η_{work} , the instantaneous scheme exhibit the highest power compression factor, but the magnitude is still far below unity ($\sim 10^{-2}$), indicating that although the power is temporally compressed, the ef-

ficiency of converting the battery' energy into high-power output remains modest.

VI. OPTIMIZATION OF DISSIPATION ENGINEERING

Finally, we analyze the optimization of dissipation engineering by tuning the modulation duration τ_2 and the minimum dissipation rate κ_{low} . Fig.4 shows the impact of these two parameters on the microwave photon generation and output characteristics of the first pulse produced under the three schemes. As shown in Fig.4(a), both

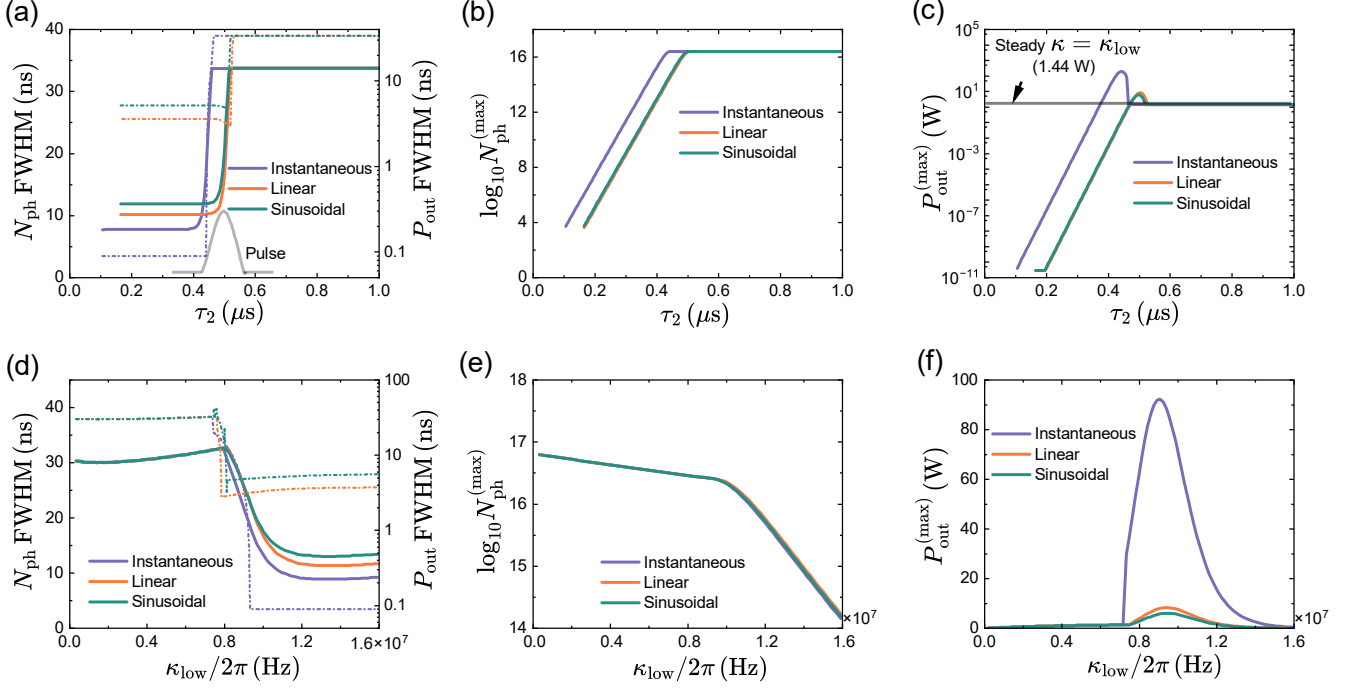


FIG. 4. Dependence of the FWHMs of the intra-cavity photon number N_{ph} (solid lines) and the microwave output P_{ins} (dashed lines), the maximum intra-cavity photon number $N_{\text{ph}}^{(\text{max})}$, and the maximum output power $P_{\text{out}}^{(\text{max})}$ on (a-c) the dissipation modulation duration τ_2 and (d-f) the minimum dissipation rate κ_{low} . In (a-c), the value of $\kappa_{\text{low}}/2\pi$ is set to 9.55×10^6 Hz; In (d-f), the values of τ_2 chosen for the instantaneous, linear and sinusoidal schemes are 440, 505 and 500 ns respectively, which yield the maximum $P_{\text{out}}^{(\text{max})}$ in (c).

FWHMs of the temporal evolutions of N_{ph} and P_{out} remain nearly constant at short τ_2 , then broaden sharply before stabilizing near their maximums. We find the abrupt broadening starts when the intra-cavity photon is accumulated close to the maximum. Therefore, the values of τ_2 (approximately 450 ns in the instantaneous schemes and 500 ns in the other two schemes) leading to the turning points of the FWHMs match those observed in Fig. 4(b), where the saturation of the maximum intra-cavity photon numbers $N_{\text{ph}}^{(\text{max})} \sim 10^{16}$ start to occur after a linear growth. Despite the similar trend of the FWHM between N_{ph} and P_{out} , the variation of the magnitude is distinct. For the intra-cavity photons, the pulse widths obtained under all schemes increase from near 10 ns to about 35 ns. In contrast, for the output, the pulse widths can change substantially by three orders of magnitude (tens of ps to more than 10 ns) in the instantaneous scheme and maximally one order of magnitude in the other two schemes. Note that factors such as the detuning between the generated microwave photons and cavity mode are not considered here. In practice, a nanosecond microwave pulse in the frequency band of GHz is feasible, however, the simulated ps-scale FWHM including both the results obtained before and after the optimization, shown in Fig. 3 and Fig. 4, implying super-broadband distributions of the photon frequencies, leads to a vast off-resonance condition. Thus, the ps-level linewidths are only of theoretical

significance, while the experimental demonstration would be largely restricted by the cavity mode linewidth.

The maximum output power $P_{\text{out}}^{(\text{max})}$ can also be dramatically affected by τ_2 as shown in Fig. 4(c). The highest $P_{\text{out}}^{(\text{max})}$ occur with the values of τ_2 chosen to be close to the ones giving rise to the turning points obtained in Figs. 4(a) and (b), which are approaching 100 W using the instantaneous protocol, and 10 W for the other protocols. It is worth noting that, due to the sharp transitions of the FWHM of P_{out} in all schemes, $P_{\text{out}}^{(\text{max})}$ is so sensitive to τ_2 that a slight extension of τ_2 beyond the optimum can significantly degrade the output power to 1.44 W, which is the same as that obtained without the dissipation modulation. We also find once τ_2 is prolonged to specific values, the further increase of τ_2 can no longer alter the intra-cavity photon characteristics and microwave output performance, and all three schemes converge to identical results.

Figs. 4(d-f) further show the optimization of the minimum dissipation rate κ_{low} based on the optimal τ_2 obtained in Fig. 4(c) which leads to the highest microwave output power. Therefore, the values of τ_2 are chosen to be 440, 505 and 500 ns for the instantaneous, linear and sinusoidal schemes respectively. As $\kappa_{\text{low}}/2\pi > 9.55 \times 10^6$ Hz, the system gradually fails to generate a complete pulse (see Fig. S2 and Fig. S3 in Appendix B), leading to a rapid decline in the maximum intra-cavity photon

number shown in Fig.4(e). Such a trend is identical for all three schemes. Meanwhile, the FWHM of N_{ph} decreases by approximately one-third of its initial value, 30 ns to a stable value around 10 ns when $\kappa_{\text{low}}/2\pi$ is increased above 7.96×10^6 Hz (see Fig.4(d)). With the increase of κ_{low} , the FWHM of the output, initially at around 30 ns, decreases to 4~6 ns for the linear and sinusoidal schemes, and further down to below 0.1 ns for the instantaneous scheme. This agrees with the dependence of the FWHM on τ_2 , consolidating the fact that the instantaneous scheme can realize much stronger temporal confinement of the output pulse. As shown in Fig.4(f), the output peak powers obtained with the three schemes are the same as those shown in Fig.4(c). The deviations of κ_{low} from its optimal value ($\kappa_{\text{low}}/2\pi = 9.55 \times 10^6$ Hz) lead to a reduction of the peak power in all schemes. Since the internal dissipation is fixed in this study, the smaller κ_{low} indicates the better energy accumulation inside the cavity while a large κ_{low} facilitates the energy extraction to external environment. The existence of the optimal κ_{low} implies the critical balance between the energy accumulation and external coupling required to optimize the output power of the coherent microwave generation in the quantum battery.

With the above optimization, we can evaluate the work extraction efficiency η_{work} and maximum power compression factor $\eta_{\text{power}}^{(\text{max})}$ in the optimal conditions. Fig.5(a) reveals that for all three schemes, beyond specific thresholds of τ_2 , η_{work} increases rapidly up to about 0.6, which is two orders of magnitude improvement compared to the non-optimized results shown in Fig.2, and then stabilizes at 0.45. The highest η_{work} achievable for all schemes are similar and the corresponding τ_2 values agree with the ones leading to the maximum intra-cavity photon numbers as discussed in Fig.4. It can be understood according to the definition of η_{work} , of which the denominator ΔE_{ph} associated with the intra-cavity photon energy is maximized. On the other hand, reducing κ_{low} can improve η_{work} as shown in Fig.5(b). It can be explained that as κ_{low} decreases, the output channel is gradually closed, so that most photon energy extracted from the quantum battery can be well accumulated in the cavity, and once the stimulated emission dominates over the internal dissipation of the cavity, the highest η_{work} can approach the unity. Nevertheless, for applications, it is undesired to always trap the photons inside the cavity, thus a certain level of dissipation to external environment is required. Despite the reduction in η_{work} , the local minimum of η_{work} appears at the optimal $\kappa_{\text{low}}/2\pi$ around 9.55×10^6 Hz which leads to the highest output power [see Fig.4(f)].

The most striking improvements due to the optimization are found in the power compression factor. Compared to the ones obtained in Fig.3, the power compression factors of all schemes can be enhanced by four to five orders of magnitude, as shown in Fig.5(c) and 5(d). The maximum power compression factors realized by the optimization are 10^3 in the instantaneous scheme, and 10^2 in the other schemes. So far, most high-power microwave

pulse compressors possess the power compression factors below 10^2 [51–54] except a time-reversal microwave pulse-compression cavity that can achieve a power compression factor of about 133[55]. Note that the values of τ_2 and κ_{low} giving rise to optimal $\eta_{\text{power}}^{(\text{max})}$ slightly differs from the ones leading to the highest output power. And significant fluctuations of $\eta_{\text{power}}^{(\text{max})}$ can be caused by the deviations of the optimal τ_2 and κ_{low} . The above observations can be attributed to the abnormal dependence of the instantaneous power P_{ins} of the quantum battery on τ_2 and κ_{low} , where substantial reduction of P_{ins} is observed near the optimal τ_2 and κ_{low} (see Fig.S4 in Appendix B).

Furthermore, we investigate the impact of the delay time τ_1 on the coherent microwave generation as shown in Fig.6. Given that the variations in τ_1 across the three schemes do not have a significant effect on the first pulse, we select the fifth pulse for comparison. Evidently, a shorter τ_1 corresponds to a higher initial photon number at the onset of modulation time τ_2 . This is because during phase τ_1 , where the dissipation rate $\kappa = \kappa_{\text{high}}$, a longer duration results in a greater reduction in the photon number. As illustrated in 6(a), the shorter delays (τ_1) tend to reduce the FWHM of the intra-cavity photon burst, while expanding τ_1 will slightly shorten the FWHM of the output pulse. In Fig.6(b), the reduction of τ_1 does not significantly affect the maximum photon number under the instantaneous scheme, however, it results in a gradual increase in the maximum intra-cavity photon number under the linear scheme. In the sinusoidal scheme, as the parameter τ_1 decreases, the maximum intra-cavity photon number initially increases until the value of τ_1 falls below 100 ns, after which it begins to decrease. This behavior can be attributed to the fact that when τ_1 becomes excessively small, the dissipation rate fails to fully undergo the complete sequence of processes τ_{down} and τ_{up} , thereby missing a portion of the mechanism responsible for photon generation. Except the FWHMs and the maximum intra-cavity microwave photon number, we find the impact of τ_1 on other parameters, e.g., the work extraction efficiency and power compression factor is negligible and is thus not presented here.

VII. DISCUSSION AND CONCLUSION

In summary, we introduce the concept of dissipation engineering as a means to dynamically control the pathways by which stored quantum battery energy is converted into propagating microwave photons. Analogous to Q-switching[56] in laser physics and to engineered reservoirs in CQED systems, dissipation engineering separates the charging and discharging stages: during charging, the system suppresses emission to accumulate energy in long-lived metastable states; during discharging, the coupling to the output channel is rapidly enhanced, enabling a burst of coherent, Purcell-enhanced microwave emission into the load. With optimal dissipation engineering, we successfully enhance the work extraction efficiency of

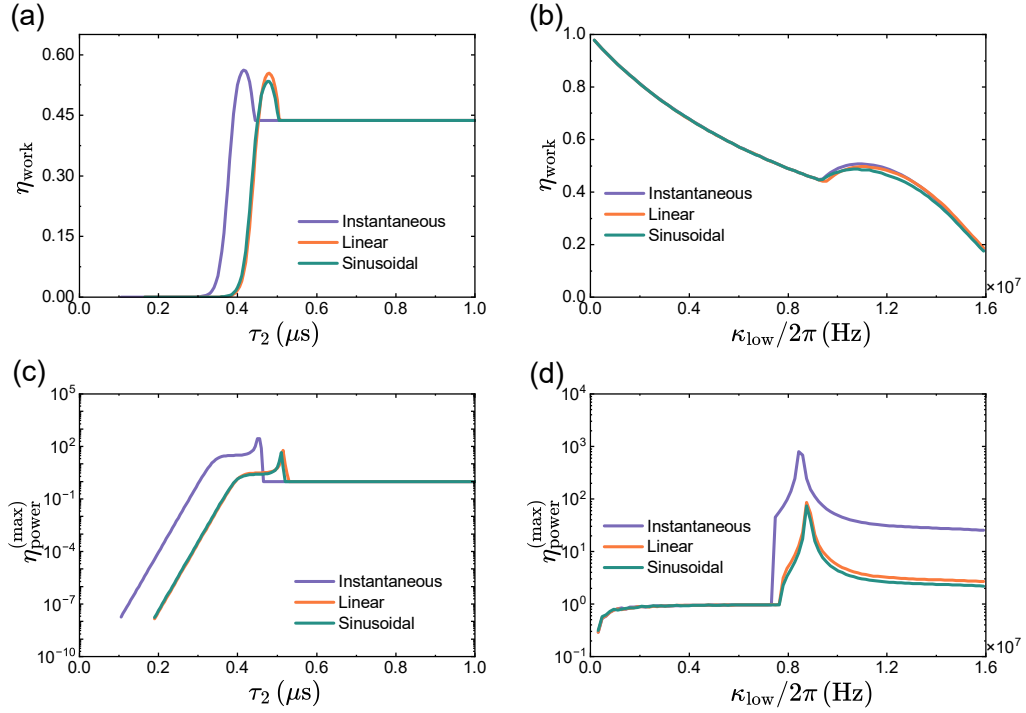


FIG. 5. (a,b) The work extraction efficiency η_{work} and (c,d) maximum power compression factor $\eta_{\text{power}}^{(\text{max})}$ depending on τ_2 and κ_{low} . In (b) and (d), τ_2 of the instantaneous, linear, and sinusoidal schemes are 440, 505 and 500 ns respectively.

the quantum battery by more than two orders of magnitude, and achieve watt-level maser output pulses with adjustable power and width. The FWHMs of the intra-cavity microwave photon burst and the output pulse can both reach the nanosecond level. In extreme cases, the FWHM of the output power can reach the order of subnanoseconds when κ undergoes an instantaneous change, while the feasibility of achieving such a short pulse experimentally is to be further investigated due to the potential mismatch between the broadband photon frequency distribution and the fixed cavity mode. Dissipation engineering near the pulse peak can significantly alter the FWHM and output power. These results demonstrate that properly timed dissipation modulation near the energy-release peak enables simultaneous control of pulse duration and intensity, thereby realizing highly efficient and temporally compressed coherent microwave emission. Especially, the power compression factors of this quantum battery is expected to surpass the state-of-the-art microwave pulse compression technique[55]. Among the three dissipation schemes compared, instantaneous scheme can achieve the smallest FWHM, the highest output power, and the highest work extraction efficiency.

From the standpoint of quantum thermodynamics, the presented strategy reflects a controlled modulation of entropy flow—temporarily isolating the battery from its dissipative environment, then selectively opening a channel that maximizes useful work extraction. By embedding this principle into the architecture of solid-state quantum batteries, our work provides a pathway to overcome

the intrinsic power limitations of maser systems and to establish a room-temperature platform for high-power coherent microwave generation. This platform may also be applicable for the microwave analogy of supercontinuum generation[57] considering the broadband output of the ultra-short pulse simulated in the instantaneous scheme. Rooted on the modulated spin-photon coupling revealed in this study, we can envision another route of dissipation engineering based on the detuning strategy, by which the spin-coupling can also be tuned with the Zeeman/Stark shift of the molecular spin states or the dielectric constant of the cavity[58] for high-power microwave output[59].

For future experimental validation, dissipation engineering can be implemented by connecting the microwave cavity to an actively controlled load for varying the external energy dissipation channel. The dissipation rate is then adjusted by controlling the coupling between the cavity and the load via a fast switch as employed in the previous cavity cooling experiments[60]. By monitoring the generated microwave photons through a detector type log amplifiers and a comparator[61], the coupling strength between the microwave cavity and the load is regulated in real time to obtain microwave pulses with a given threshold.

Acknowledgements.—The work is supported by the National Natural Science Foundation of China (Grant No. 12204040 and 12574382), and the Beijing Institute of Technology Research Fund Program for Young Scholars (Grant No. XSQD-6120230016).

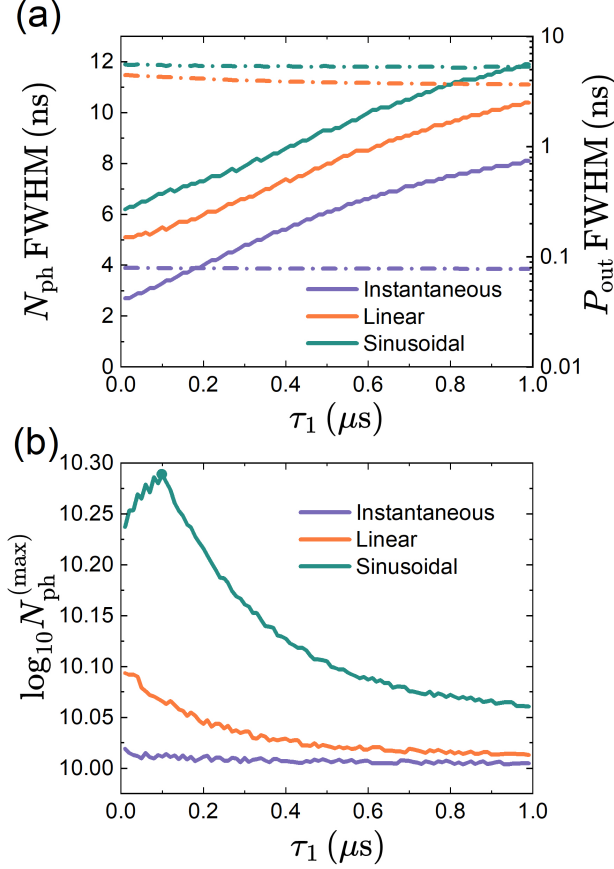


FIG. 6. (a) Variations of the FWHMs of N_{ph} (solid lines) and P_{out} (dashed lines) of the fifth output pulse with the delay time τ_1 . (b) The influence of τ_1 on the maximum photon number $N_{\text{ph}}^{(\text{max})}$ of the fifth pulse.

Appendix A: MASTER EQUATION

The complete dynamics of the quantum battery are described by [32, 42]:

$$\begin{aligned}
 \partial_t \hat{\rho} = & -\frac{i}{\hbar} [\hat{H}_{\text{bat}} + \hat{H}_{\text{m}} + \hat{H}_{\text{m-bat}}, \hat{\rho}] \\
 & + \frac{1}{2} \xi \sum_{\mathbf{k}} \mathcal{D}[\hat{\sigma}_{\mathbf{k}}^{21}] \hat{\rho} + \frac{1}{2} (\xi + k_{\text{sp}}) \sum_{\mathbf{k}} \mathcal{D}[\hat{\sigma}_{\mathbf{k}}^{12}] \hat{\rho} \\
 & + \sum_{\mathbf{k}} \left(\sum_{i=3,4,5} \frac{1}{2} k_{2i} \mathcal{D}[\hat{\sigma}_{\mathbf{k}}^{i2}] \hat{\rho} + \sum_{i=3,4,5} \frac{1}{2} k_{i1} \mathcal{D}[\hat{\sigma}_{\mathbf{k}}^{1i}] \hat{\rho} \right) \\
 & + \sum_{\mathbf{k}} \sum_{i,j=3,4,5; i \neq j} \left(\frac{1}{2} k_{ij} \mathcal{D}[\hat{\sigma}_{\mathbf{k}}^{ji}] \hat{\rho} \right) \\
 & + \sum_{\mathbf{k}} \sum_{i,j=3,4,5; i < j} \left(\frac{1}{4} \chi_{ij} \mathcal{D}[\hat{\sigma}_{\mathbf{k}}^{ij} - \hat{\sigma}_{\mathbf{k}}^{ji}] \hat{\rho} \right) \\
 & + \frac{\kappa}{2} [(n_{\text{m}}^{\text{th}} + 1) \mathcal{D}[\hat{a}] \hat{\rho} + n_{\text{m}}^{\text{th}} \mathcal{D}[\hat{a}^\dagger] \hat{\rho}],
 \end{aligned}$$

with the Lindblad superoperator $\mathcal{D}[\hat{O}] \hat{\rho} = 2\hat{O} \hat{\rho} \hat{O}^\dagger - \hat{O}^\dagger \hat{O} \hat{\rho} - \hat{\rho} \hat{O}^\dagger \hat{O}$. The second through sixth lines sequentially present all components of the Lindblad superoperator $\mathcal{L}[\hat{\rho}]$ introduced in the main text, namely the optical pumping and the spontaneous emission, the inter-system crossing, the spin-lattice relaxation, the dephasing process, and the thermal emission or excitation of the microwave cavity. The optical pumping employed for the quantum battery is a 2×10^4 W laser. (See Table I for parameter definitions.) The derived system of equations necessary for analyzing the discharge process is characterized by:

$$\begin{aligned}
 \frac{d}{dt} \langle \hat{\sigma}_1^{11} \rangle = & -\xi \langle \hat{\sigma}_1^{11} \rangle + (\xi + k_{\text{sp}}) \langle \hat{\sigma}_1^{22} \rangle + k_{31} \langle \hat{\sigma}_1^{33} \rangle \\
 & + k_{41} \langle \hat{\sigma}_1^{44} \rangle + k_{51} \langle \hat{\sigma}_1^{55} \rangle \\
 \frac{d}{dt} \langle \hat{\sigma}_1^{22} \rangle = & \xi \langle \hat{\sigma}_1^{11} \rangle - (\xi + k_{\text{sp}}) \langle \hat{\sigma}_1^{22} \rangle - k_{23} \langle \hat{\sigma}_1^{22} \rangle - k_{24} \langle \hat{\sigma}_1^{22} \rangle \\
 & - k_{25} \langle \hat{\sigma}_1^{22} \rangle \\
 \frac{d}{dt} \langle \hat{\sigma}_1^{33} \rangle = & ig_{35} (\langle \hat{\sigma}_1^{53} \hat{a} \rangle - \langle \hat{a}^\dagger \hat{\sigma}_1^{35} \rangle) + k_{23} \langle \hat{\sigma}_1^{22} \rangle - k_{31} \langle \hat{\sigma}_1^{33} \rangle \\
 & - k_{34} \langle \hat{\sigma}_1^{33} \rangle + k_{43} \langle \hat{\sigma}_1^{44} \rangle - k_{35} \langle \hat{\sigma}_1^{33} \rangle + k_{53} \langle \hat{\sigma}_1^{55} \rangle \\
 \frac{d}{dt} \langle \hat{\sigma}_1^{44} \rangle = & k_{24} \langle \hat{\sigma}_1^{22} \rangle - k_{41} \langle \hat{\sigma}_1^{44} \rangle + k_{34} \langle \hat{\sigma}_1^{33} \rangle - k_{43} \langle \hat{\sigma}_1^{44} \rangle \\
 & - k_{45} \langle \hat{\sigma}_1^{44} \rangle + k_{54} \langle \hat{\sigma}_1^{55} \rangle \\
 \frac{d}{dt} \langle \hat{\sigma}_1^{55} \rangle = & ig_{35} (\langle \hat{a}^\dagger \hat{\sigma}_1^{35} \rangle - \langle \hat{\sigma}_1^{53} \hat{a} \rangle) + k_{25} \langle \hat{\sigma}_1^{22} \rangle - k_{51} \langle \hat{\sigma}_1^{55} \rangle \\
 & + k_{35} \langle \hat{\sigma}_1^{33} \rangle - k_{53} \langle \hat{\sigma}_1^{55} \rangle + k_{45} \langle \hat{\sigma}_1^{44} \rangle - k_{54} \langle \hat{\sigma}_1^{55} \rangle \\
 \frac{d}{dt} \langle \hat{a}^\dagger \hat{a} \rangle = & Nig_{35} (\langle \hat{\sigma}_1^{53} \hat{a} \rangle - \langle \hat{a}^\dagger \hat{\sigma}_1^{35} \rangle) - \kappa \langle \hat{a}^\dagger \hat{a} \rangle \\
 \frac{d}{dt} \langle \hat{a}^\dagger \hat{\sigma}_1^{35} \rangle = & i\omega_{\text{m}} \langle \hat{a}^\dagger \hat{\sigma}_1^{35} \rangle - i\omega_{35} \langle \hat{a}^\dagger \hat{\sigma}_1^{35} \rangle + ig_{35} (N-1) \langle \hat{\sigma}_1^{53} \hat{\sigma}_2^{35} \rangle \\
 & + ig_{35} [(1 + \langle \hat{a}^\dagger \hat{a} \rangle) \langle \hat{\sigma}_1^{55} \rangle - \langle \hat{a}^\dagger \hat{a} \rangle \langle \hat{\sigma}_1^{33} \rangle] \\
 & - \frac{1}{2} k_{31} \langle \hat{a}^\dagger \hat{\sigma}_1^{35} \rangle - \frac{1}{2} k_{51} \langle \hat{a}^\dagger \hat{\sigma}_1^{35} \rangle - \frac{1}{2} k_{34} \langle \hat{a}^\dagger \hat{\sigma}_1^{35} \rangle \\
 & - \frac{1}{2} k_{35} \langle \hat{a}^\dagger \hat{\sigma}_1^{35} \rangle - \frac{1}{2} k_{53} \langle \hat{a}^\dagger \hat{\sigma}_1^{35} \rangle - \frac{1}{2} k_{54} \langle \hat{a}^\dagger \hat{\sigma}_1^{35} \rangle \\
 & - \frac{1}{4} \chi_{34} \langle \hat{a}^\dagger \hat{\sigma}_1^{35} \rangle - \chi_{35} \langle \hat{a}^\dagger \hat{\sigma}_1^{35} \rangle - \frac{1}{4} \chi_{45} \langle \hat{a}^\dagger \hat{\sigma}_1^{35} \rangle \\
 & - \frac{\kappa}{2} \langle \hat{a}^\dagger \hat{\sigma}_1^{35} \rangle \\
 \frac{d}{dt} \langle \hat{\sigma}_1^{53} \hat{\sigma}_2^{35} \rangle = & ig_{35} \langle \hat{a} \hat{\sigma}_1^{53} \rangle (\langle \hat{\sigma}_2^{55} \rangle - \langle \hat{\sigma}_2^{33} \rangle) \\
 & + ig_{35} \langle \hat{a}^\dagger \hat{\sigma}_1^{35} \rangle (\langle \hat{\sigma}_2^{33} \rangle - \langle \hat{\sigma}_2^{55} \rangle) - k_{31} \langle \hat{\sigma}_1^{53} \hat{\sigma}_2^{35} \rangle \\
 & - k_{51} \langle \hat{\sigma}_1^{53} \hat{\sigma}_2^{35} \rangle - k_{34} \langle \hat{\sigma}_1^{53} \hat{\sigma}_2^{35} \rangle - k_{35} \langle \hat{\sigma}_1^{53} \hat{\sigma}_2^{35} \rangle \\
 & - k_{53} \langle \hat{\sigma}_1^{53} \hat{\sigma}_2^{35} \rangle - k_{54} \langle \hat{\sigma}_1^{53} \hat{\sigma}_2^{35} \rangle - \frac{1}{2} \chi_{34} \langle \hat{\sigma}_1^{53} \hat{\sigma}_2^{35} \rangle \\
 & - 2\chi_{35} \langle \hat{\sigma}_1^{53} \hat{\sigma}_2^{35} \rangle - \frac{1}{2} \chi_{45} \langle \hat{\sigma}_1^{53} \hat{\sigma}_2^{35} \rangle.
 \end{aligned}$$

The contribution of thermal equilibrium photons is neglected in the above equation, as their number is negligible relative to the number of generated microwave photons.

Descriptions	Symbols	Values	Descriptions	Symbols	Values
Resonator frequency	$\omega_m/2\pi$	1.45 GHz	Thermal equilibrium photon number	n_m^{th}	4000
Spin-resonator coupling	$g_{35}/2\pi$	3.66×10^{-2} Hz[40]	Number of spins	N_{pen}	1×10^{17}
Spin transition frequency	$\omega_{35}/2\pi$	1.45 GHz	Spin dephasing rates	$(\chi_{35} \approx \chi_{34} \approx \chi_{45})/2\pi$	0.18 MHz[40]
Spontaneous emission rate	k_{sp}	42 MHz[62]	Optical pumping rate	ξ	3.1 kHz/W[63]
Spin-lattice relaxation rates	k_{35}	1.1×10^4 Hz[40]		k_{34}	2.8×10^4 Hz[40]
	k_{45}	0.4×10^4 Hz[40]			
	k_{25}	52.4 MHz[63]		k_{24}	11 MHz[63]
Intersystem crossing rates	k_{23}	5.52 MHz[63]		k_{51}	2.2×10^4 Hz[40]
	k_{41}	1.4×10^4 Hz[40]		k_{31}	0.2×10^4 Hz[40]
Highest photon dissipation rate	$\kappa_{\text{high}}/2\pi$	1.45×10^3 MHz	Lowest photon dissipation rate	$\kappa_{\text{low}}/2\pi$	9.55 MHz

TABLE I. Summary of the parameters involved in the dynamics of the pentacene molecular quantum battery in Fig.S1.

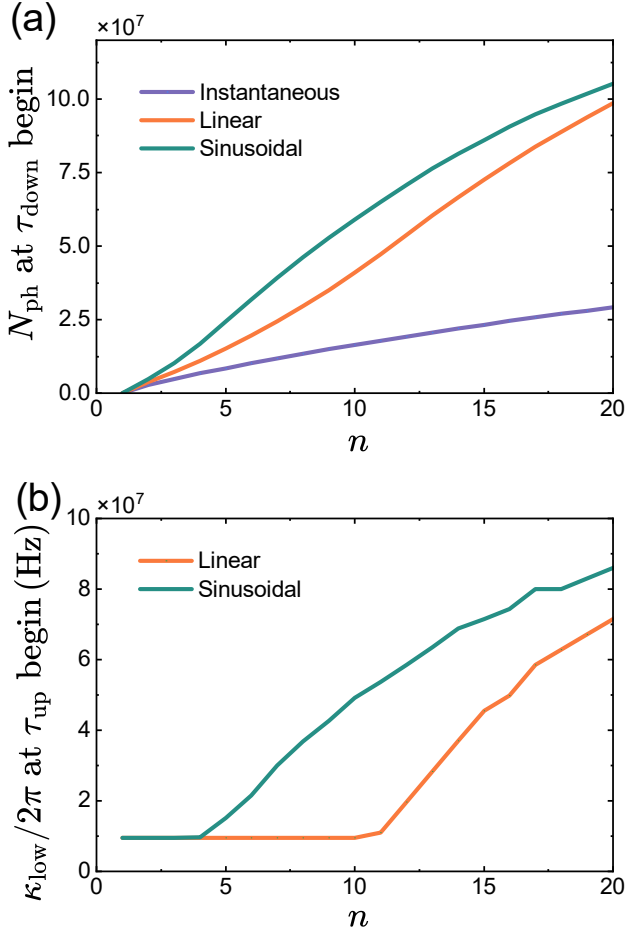


FIG. S1. (a) N_{ph} at the start of the τ_{down} (or τ_2) stage in the n th cycle. (b) κ at the start of the τ_{up} state ($N_{\text{ph}} = 10^{10}$). The parameters are identical to those presented in Fig.1 of the main text, with $\tau_1 = 1 \times 10^{-8}$ s, $\tau_{\text{down}} = 2/\kappa_{\text{low}}$, and $\tau_{\text{up}} = \tau_{\text{down}}$. The laser power is set at 2×10^4 W, with all other parameters summarized in Table.I.

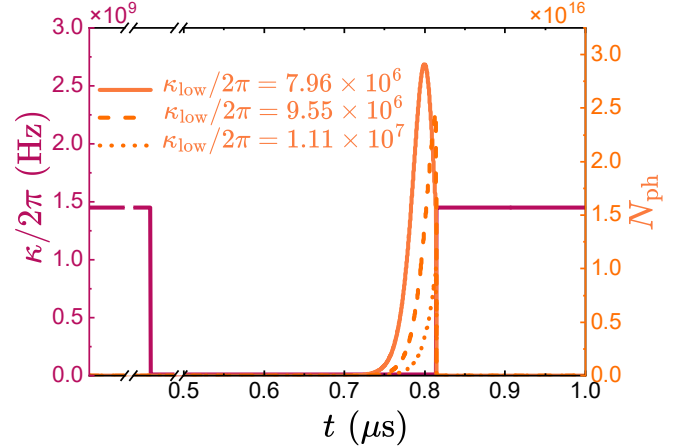


FIG. S2. The dissipation rate κ and photon number N_{ph} vary with t at different κ_{low} values under the instantaneous scheme.

Appendix B: SIMULATION OF THE DISCHARGING DYNAMICS

In the three regulation schemes, the photon number N_{ph} at the beginning of each control cycle increases progressively, as shown in Fig.S1(a). This behavior accounts for the observed reduction in the FWHM in Fig.2 of the main text. In Fig.S1(b), for the linear scheme, $\kappa/2\pi = \kappa_{\text{low}}/2\pi$ (9.55×10^6 Hz) during the first 10 cycles upon entering stage τ_{up} , but $\kappa > \kappa_{\text{low}}$ thereafter. This indicates that the photon number reached the predefined threshold 10^{10} in stage τ_{down} after 10 cycles, bypassing stage τ_{low} and without completing stage τ_{down} (τ_{up}). Similarly, for the sinusoidal scheme, the photon number attained the threshold in stage τ_{down} after the 4th cycle. Since stage τ_{up} was not fully completed in either case, the maximum photon number began to decrease after the 10th cycle for the linear scheme and after the 4th cycle for the sinusoidal scheme, as illustrated in Fig.2(e) and Fig.2(f) in the main text.

Fig.S2 presents the evolution of both the dissipation rate and photon population over time, under the transient protocol with different κ_{low} . When $\kappa/2\pi = 7.96 \times 10^6$ Hz,

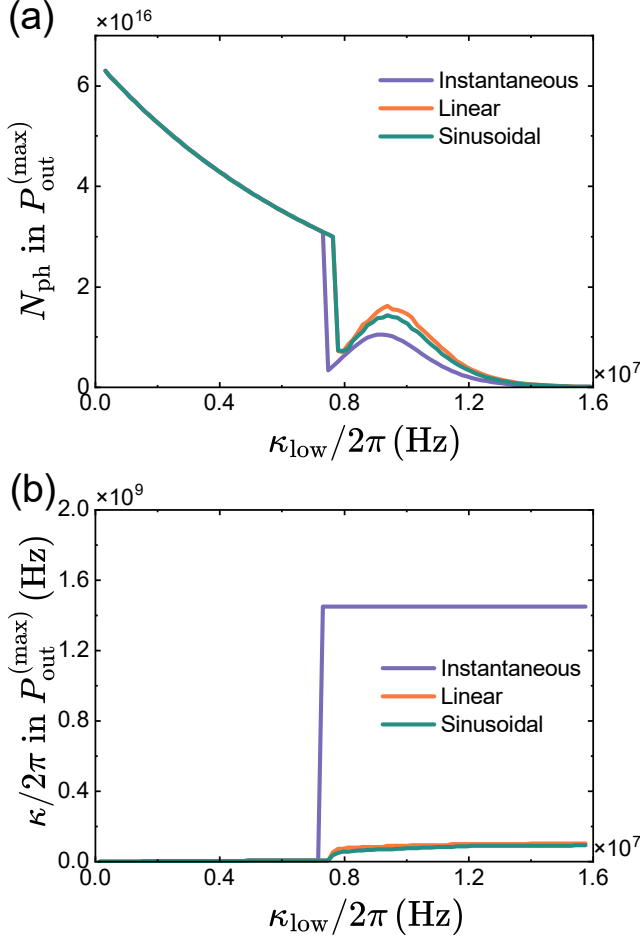


FIG. S3. (a) N_{ph} and (b) κ at maximum power $P_{\text{out}}^{(\text{max})}$ for different κ_{low} . All parameters are identical to those in Fig. 4.

the microwave photon pulse can still reach its peak; when $\kappa/2\pi = 9.55 \times 10^6$ Hz, the number of generated microwave photons cannot reach the peak of the pulse; and when $\kappa/2\pi = 1.11 \times 10^7$ Hz, the number of generated microwave photons is less than half of the peak. Therefore, near $\kappa/2\pi = 9.55 \times 10^6$ Hz, especially after $\kappa/2\pi > 9.55 \times 10^6$ Hz, the microwave optical pulses become increasingly incomplete, resulting in the rapid decline of the maximum photon number shown in Fig. 4(e) of the main text.

Fig. S3 illustrates the photon number N_{ph} and dissipa-

tion rate κ at maximum power across various values of parameter κ_{low} . When $\kappa/2\pi < 7.16 \times 10^6$ Hz, the first pulse can be fully observed, allowing N_{ph} to reach its maximum value, with $\kappa = \kappa_{\text{low}}$ at $P_{\text{out}}^{(\text{max})}$. Subsequently, only a partial area of the first pulse can be obtained gradually, leading to a rapid decrease in N_{ph} while κ at $P_{\text{out}}^{(\text{max})}$ increases accordingly. The instantaneous scheme corresponds directly to $\kappa = \kappa_{\text{high}}$, and consequently, as illustrated in Fig. 4(f), the output power achieves its maximum value at $\kappa/2\pi = 9.55 \times 10^6$ Hz.

In Fig. S4(a) and Fig. S4(b), as parameters τ_2 or κ_{low} increase, when the position of the maximum output power $P_{\text{out}}^{(\text{max})}$ approaches the peak of the microwave photon pulse, the corresponding instantaneous power P_{ins} first decreases and then increases. The underlying mechanism of this phenomenon can be understood with reference to Fig. S4(c). Instantaneous power is the rate of change of energy, and the change in energy is basically opposite to the change in the number of photons.

Taking κ_{low} as an example, as κ_{low} gradually increases, the acquired microwave pulse becomes increasingly incomplete. The position of $P_{\text{out}}^{(\text{max})}$ shifts from the vicinity of the peak of the microwave optical pulse to the transition point between stage τ_{low} and stage τ_{up} (or new stage τ_1)—corresponding to the boundary between region 2 and region 3 in Fig. S4(c). This shift aligns with a sudden change in instantaneous power observed in region 3 of Fig. S4(b). As κ_{low} continues to increase, the position of $P_{\text{out}}^{(\text{max})}$ shifts through the peak of the microwave optical pulse, resulting in an initial decrease followed by an increase in instantaneous power (see region 2 in Fig. S4(b) and Fig. S4(c)). When the photon number at $P_{\text{out}}^{(\text{max})}$ reaches approximately half of the peak value of the entire microwave optical pulse, the instantaneous power exhibits a transient increase followed by a decrease (see region 1 in Fig. S4(b) and Fig. S4(c)).

As the parameter τ_2 increases, the sequence in which each region appears is reversed. In the process of progressively generating a complete microwave optical pulse, region 1 is encountered first, followed by regions 2 and 3, as illustrated in Fig. S4(a). The variation in instantaneous power constitutes the primary factor responsible for the observed changes in parameters η_{work} and η_{power} depicted in Fig. 5(c) and 5(d).

- [1] R. Alicki and M. Fannes, Entanglement boost for extractable work from ensembles of quantum batteries, *Phys. Rev. E* **87**, 042123 (2013).
- [2] F. Campaioli, S. Gherardini, J. Q. Quach, M. Polini, and G. M. Andolina, Colloquium: Quantum batteries, *Rev. Mod. Phys.* **96**, 031001 (2024).
- [3] J. Joshi and T. S. Mahesh, Experimental investigation of a quantum battery using star-topology nmr spin systems, *Phys. Rev. A* **106**, 042601 (2022).
- [4] Z. Niu, Y. Wu, Y. Wang, X. Rong, and J. Du, Experi-

mental investigation of coherent ergotropy in a single spin system, *Phys. Rev. Lett.* **133**, 180401 (2024).

- [5] W.-L. Song, J.-L. Wang, B. Zhou, W.-L. Yang, and J.-H. An, Self-discharging mitigated quantum battery, *Phys. Rev. Lett.* **135**, 020405 (2025).
- [6] C.-K. Hu, J. Qiu, P. J. P. Souza, J. Yuan, Y. Zhou, L. Zhang, J. Chu, X. Pan, L. Hu, J. Li, Y. Xu, Y. Zhong, S. Liu, F. Yan, D. Tan, R. Bachelard, C. J. Villas-Boas, A. C. Santos, and D. Yu, Optimal charging of a superconducting quantum battery, *Quantum Sci. Technol.* **7**,

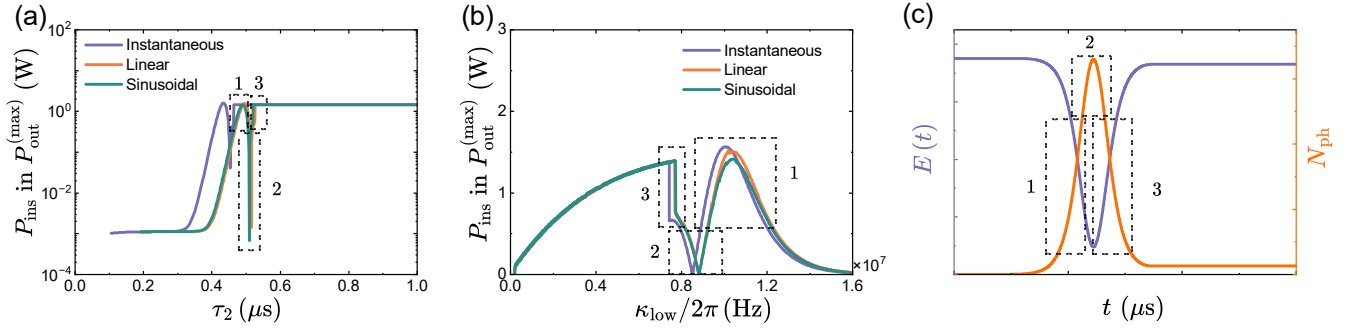


FIG. S4. P_{ins} at maximum power $P_{\text{out}}^{(\text{max})}$ for different (a) τ_2 or (b) κ_{low} . All parameters are identical to those in Fig. 5. (c) Schematic diagram of the energy and photon number dynamics during quantum battery operation. Different regions indicate the position of photons on the pulse when the output power reaches its maximum value.

- 045018 (2022).
- [7] A. Rojo-Francàs, F. Isaule, A. C. Santos, B. Juliá-Díaz, and N. T. Zinner, Stable collective charging of ultracold-atom quantum batteries, *Phys. Rev. A* **110**, 032205 (2024).
 - [8] J. Q. Quach, K. E. McGhee, L. Ganzer, D. M. Rouse, B. W. Lovett, E. M. Gauger, J. Keeling, G. Cerullo, D. G. Lidzey, and T. Virgili, Superabsorption in an organic microcavity: Toward a quantum battery, *Sci. Adv.* **8**, eabk3160 (2022).
 - [9] J. Li and N. Wu, Collective charging of an organic quantum battery, *Phys. Rev. E* **111**, 044118 (2025).
 - [10] D. J. Tibben, E. Della Gaspera, J. van Embden, P. Reinck, J. Q. Quach, F. Campaioli, and D. E. Gómez, Extending the self-discharge time of dicke quantum batteries using molecular triplets, *PRX Energy* **4**, 023012 (2025).
 - [11] K. Hymas, J. B. Muir, D. Tibben, J. van Embden, T. Hirai, C. J. Dunn, D. E. Gómez, J. A. Hutchison, T. A. Smith, and J. Q. Quach, *Experimental demonstration of a scalable room-temperature quantum battery* (2025), [arXiv:2501.16541](https://arxiv.org/abs/2501.16541).
 - [12] M. H. Devoret and R. J. Schoelkopf, Superconducting circuits for quantum information: An outlook, *Science* **339**, 1169 (2013).
 - [13] M. Saffman, Quantum computing with atomic qubits and rydberg interactions: progress and challenges, *J. Phys. B: At., Mol. Opt. Phys.* **49**, 202001 (2016).
 - [14] T. P. Harty, D. T. C. Allcock, C. J. Ballance, L. Guidoni, H. A. Janacek, N. M. Linke, D. N. Stacey, and D. M. Lucas, High-fidelity preparation, gates, memory, and read-out of a trapped-ion quantum bit, *Phys. Rev. Lett.* **113**, 220501 (2014).
 - [15] V. Dobrovitski, G. Fuchs, A. Falk, C. Santori, and D. Awschalom, Quantum control over single spins in diamond, *Annu. Rev. Condens. Matter Phys.* **4**, 23 (2013).
 - [16] T. Xie, Z. Zhao, S. Xu, X. Kong, Z. Yang, M. Wang, Y. Wang, F. Shi, and J. Du, 99.92%-fidelity cnot gates in solids by noise filtering, *Phys. Rev. Lett.* **130**, 030601 (2023).
 - [17] J. C. Bardin, D. H. Slichter, and D. J. Reilly, Microwaves in quantum computing, *IEEE Journal of Microwaves* **1**, 403 (2021).
 - [18] Y. Wang, H. Wu, and Q. Zhao, Metastability-induced solid-state quantum batteries for powering microwave quantum electronics, *Phys. Rev. A* **112**, L030201 (2025).
 - [19] A. A. Belyaev, V. G. Voronzov, N. A. Demidov, K. Y. Khabarova, and N. N. Kolachevsky, N g basov's legacy: from the first masers to optical frequency standards, *Phys. Usp.* **66**, 1026 (2023).
 - [20] M. Ballu, B. Mirmand, T. Badr, H. Perrin, and A. Perrin, Fast manipulation of a quantum gas on an atom chip with a strong microwave field, *Phys. Rev. A* **110**, 053312 (2024).
 - [21] F. N. M. Froning, L. C. Camenzind, O. A. H. van der Molen, A. Li, E. P. A. M. Bakkers, D. M. Zumbühl, and F. R. Braakman, Ultrafast hole spin qubit with gate-tunable spin-orbit switch functionality, *Nat. Nanotechnol.* **16**, 308 (2021).
 - [22] E. I. Rosenthal, C. P. Anderson, H. C. Kleidermacher, A. J. Stein, H. Lee, J. Grzesik, G. Scuri, A. E. Rugar, D. Riedel, S. Aghaeimeibodi, G. H. Ahn, K. Van Gasse, and J. Vučković, Microwave spin control of a tin-vacancy qubit in diamond, *Phys. Rev. X* **13**, 031022 (2023).
 - [23] N. Aslam, M. Pfender, R. Stöhr, P. Neumann, M. Scheffler, H. Sumiya, H. Abe, S. Onoda, T. Ohshima, J. Isoya, and J. Wrachtrup, Single spin optically detected magnetic resonance with 60–90 ghz (e-band) microwave resonators, *Rev. Sci. Instrum.* **86**, 064704 (2015).
 - [24] E. I. Rosenthal, S. Biswas, G. Scuri, H. Lee, A. J. Stein, H. C. Kleidermacher, J. Grzesik, A. E. Rugar, S. Aghaeimeibodi, D. Riedel, M. Titze, E. S. Bielejec, J. Choi, C. P. Anderson, and J. Vučković, Single-shot readout and weak measurement of a tin-vacancy qubit in diamond, *Phys. Rev. X* **14**, 041008 (2024).
 - [25] M. Ohkuma, E. Kimura, E. Lee, R. Matsumoto, S. Ohyama, S. Tsuchiya, H. Lim, Y. S. Lee, Y. Takano, J. Lee, and K. Arai, *Coherent control of solid-state defect spins via patterned boron-doped diamond circuit* (2025), [arXiv:2412.15586](https://arxiv.org/abs/2412.15586).
 - [26] A. J. Ramsay, R. Hekmati, C. J. Patrickson, S. Baber, D. R. M. Arvidsson-Shukur, A. J. Bennett, and I. J. Luxmoore, Coherence protection of spin qubits in hexagonal boron nitride, *Nat. Commun.* **14**, 461 (2023).
 - [27] G. M. Andolina, M. Keck, A. Mari, M. Campisi, V. Giovannetti, and M. Polini, Extractable work, the role of correlations, and asymptotic freedom in quantum batteries, *Phys. Rev. Lett.* **122**, 047702 (2019).
 - [28] J.-Y. Gyhm and U. R. Fischer, Beneficial and detrimental entanglement for quantum battery charging, *AVS Quantum Sci.* **6**, 012001 (2024).
 - [29] F. Pirmoradian and K. Mølmer, Aging of a quantum battery, *Phys. Rev. A* **100**, 043833 (2019).

- [30] K. Xu, H.-G. Li, H.-J. Zhu, and W.-M. Liu, Inhibiting the self-discharging process of quantum batteries in non-markovian noises, *Phys. Rev. E* **109**, 054132 (2024).
- [31] A. C. Santos, Quantum advantage of two-level batteries in the self-discharging process, *Phys. Rev. E* **103**, 042118 (2021).
- [32] J. D. Breeze, E. Salvadori, J. Sathian, N. M. Alford, and C. W. M. Kay, Room-temperature cavity quantum electrodynamics with strongly coupled dicke states, *npj Quantum Inf.* **3**, 40 (2017).
- [33] C. W. Zollitsch, S. Ruloff, Y. Fett, H. T. A. Wiedemann, R. Richter, J. D. Breeze, and C. W. M. Kay, Maser threshold characterization by resonator q-factor tuning, *Commun. Phys.* **6**, 295 (2023).
- [34] J. F. Poyatos, J. I. Cirac, and P. Zoller, Quantum reservoir engineering with laser cooled trapped ions, *Phys. Rev. Lett.* **77**, 4728 (1996).
- [35] D. Marcos, A. Tomadin, S. Diehl, and P. Rabl, Photon condensation in circuit quantum electrodynamics by engineered dissipation, *New J. Phys.* **14**, 055005 (2012).
- [36] S. Pontula, S. Vaidya, C. Roques-Carmes, S. Z. Uddin, M. Soljačić, and Y. Salamin, Non-reciprocal frequency conversion in a non-hermitian multimode nonlinear system, *Nat. Commun.* **16**, 7544 (2025).
- [37] X. Lv, B. Nie, C. Yang, R. Ma, Z. Wang, Y. Liu, X. Jin, K. Zhu, Z. Chen, D. Qian, G. Zhang, G. Lv, Q. Gong, F. Bo, and Q.-F. Yang, Broadband microwave-rate dark pulse microcombs in dissipation-engineered linbo3 microresonators, *Nat. Commun.* **16**, 2389 (2025).
- [38] D. J. Sloop, H. Yu, T. Lin, and S. I. Weissman, Electron spin echoes of a photoexcited triplet: Pentacene in p-terphenyl crystals, *J. Chem. Phys.* **75**, 3746 (1981).
- [39] M. Oxborrow, J. D. Breeze, and N. M. Alford, Room-temperature solid-state maser, *Nature* **488**, 353 (2012).
- [40] H. Wu, X. Xie, W. Ng, S. Mehanna, Y. Li, M. Attwood, and M. Oxborrow, Room-temperature quasi-continuous-wave pentacene maser pumped by an invasive Ce : YAG luminescent concentrator, *Phys. Rev. Appl.* **14**, 064017 (2020).
- [41] Y. Shimony, Z. Burshtein, A.-A. Baranga, Y. Kalisky, and M. Strauss, Repetitive q-switching of a cw nd:yag laser using cr/sup 4+/:yag saturable absorbers, *IEEE J. Quantum Electron.* **32**, 305 (1996).
- [42] Q. Wu, Y. Zhang, H. Wu, S.-L. Su, K.-K. Liu, M. Oxborrow, C.-X. Shan, and K. Mølmer, Theoretical study of superradiant masing with solid-state spins at room temperature, *Sci. China:Phys., Mech. Astron.* **67**, 260314 (2024).
- [43] D. Kajfez and P. Guillon, *Dielectric Resonators*, Artech House microwave library (Noble Publishing Corporation, 1998).
- [44] F. Krausz, M. Fermann, T. Brabec, P. Curley, M. Hofer, M. Ober, C. Spielmann, E. Wintner, and A. Schmidt, Femtosecond solid-state lasers, *IEEE J. Quantum Electron.* **28**, 2097 (1992).
- [45] E. Salvadori, J. D. Breeze, K.-J. Tan, J. Sathian, B. Richards, M. W. Fung, G. Wolfowicz, M. Oxborrow, N. M. Alford, and C. W. M. Kay, Nanosecond time-resolved characterization of a pentacene-based room-temperature maser, *Sci. Rep.* **7**, 41836 (2017).
- [46] H. Wu, S. Mirkhanov, W. Ng, K.-C. Chen, Y. Xiong, and M. Oxborrow, Invasive optical pumping for room-temperature masers, time-resolved epr, triplet-dnp, and quantum engines exploiting strong coupling, *Opt. Express* **28**, 29691 (2020).
- [47] J. Breeze, K.-J. Tan, B. Richards, J. Sathian, M. Oxborrow, and N. M. Alford, Enhanced magnetic purcell effect in room-temperature masers, *Nat. Commun.* **6**, 6215 (2015).
- [48] S. Long, P. Choubey, M. Attwood, J. Chang, H. Torun, and J. Sathian, *Feasibility of free-space transmission using l-band maser signals in organic gain media* (2025), [arXiv:2511.09059](#).
- [49] S. Long, M. Attwood, J. Chang, P. Choubey, H. Torun, and J. Sathian, *L-band milliwatt room-temperature solid-state maser* (2025), [arXiv:2511.09056](#).
- [50] H. Sixl and M. Schwoerer, Dynamics of optical electron spin-polarization in naphthalene. magnetic field effects on phosphorescence, *Chem. Phys. Lett.* **6**, 21 (1970).
- [51] Z. Zhang, R. Pan, W. Wang, Y. Yao, W. Jiang, Z. Wu, Y. Pu, J. Wang, Y. Luo, and G. Liu, Increasing the power compression factor by overmoded waveguide for subnanosecond microwave pulse generation, *IEEE Trans. Electron Devices* **72**, 1435 (2025).
- [52] S. V. Samsonov, A. D. R. Phelps, V. L. Bratman, G. Burt, G. G. Denisov, A. W. Cross, K. Ronald, W. He, and H. Yin, Compression of frequency-modulated pulses using helically corrugated waveguides and its potential for generating multigigawatt rf radiation, *Phys. Rev. Lett.* **92**, 118301 (2004).
- [53] L. Zhang, S. V. Mishakin, W. He, S. V. Samsonov, M. McStravick, G. G. Denisov, A. W. Cross, V. L. Bratman, C. G. Whyte, C. W. Robertson, A. R. Young, K. Ronald, and A. D. R. Phelps, Experimental study of microwave pulse compression using a five-fold helically corrugated waveguide, *IEEE Trans. Microwave Theory Tech.* **63**, 1090 (2015).
- [54] Z. Zhang, R. Pan, W. Wang, G. Liu, Y. Yao, W. Jiang, Z. Wu, Y. Pu, J. Wang, and Y. Luo, Sub-nanosecond microwave passive pulse generation with high power compression factor using structural reflection, *IEEE Electron Device Lett.* **45**, 1317 (2024).
- [55] Z. B. Drikas, B. D. Addissie, V. M. Mendez, and S. Raman, A compact, high-gain, high-power, ultrawideband microwave pulse compressor using time-reversal techniques, *IEEE Trans. Microwave Theory Tech.* **68**, 3355 (2020).
- [56] F. J. McClung and R. W. Hellwarth, Giant optical pulsations from ruby, *Appl. Opt.* **1**, 103 (1962).
- [57] C.-S. Brès, A. D. Torre, D. Grassani, V. Brasch, C. Grillet, and C. Monat, Supercontinuum in integrated photonics: generation, applications, challenges, and perspectives, *Nanophotonics* **12**, 1199 (2023).
- [58] M. Shlafman, I. Bayn, and J. Salzman, Effect of dielectric constant tuning on a photonic cavity frequency and q-factor, *Opt. Express* **18**, 15907 (2010).
- [59] D. Ziemkiewicz and S. Zielińska-Raczyńska, Solid-state pulsed microwave emitter based on rydberg excitons, *Opt. Express* **27**, 16983 (2019).
- [60] K.-C. Chen and M. Oxborrow, *Overcoming the thermal-noise limit of microwave measurements by pre-cooling with an active cold load* (2024), [arXiv:2408.05371 \[quant-ph\]](#).
- [61] G. R. Shankar Reddy and A. Bharathi, Successive detection logarithmic amplifier for ecm features of radar, in *2023 3rd International Conference on Intelligent Technologies (CONIT)* (2023) pp. 1–6.
- [62] K. Takeda, K. Takegoshi, and T. Terao, Zero-field electron spin resonance and theoretical studies of light penetration

into single crystal and polycrystalline material doped with molecules photoexcitable to the triplet state via intersystem crossing, [J. Chem. Phys.](#) **117**, 4940 (2002).

[63] H. Wu, S. Mirkhanov, W. Ng, and M. Oxborrow, Bench-

top cooling of a microwave mode using an optically pumped spin refrigerator, [Phys. Rev. Lett.](#) **127**, 053604 (2021).